ELSEVIER

International Journal of Heat and Fluid Flow 22 (2001) 72–81

International Journal of HEAT AND FLUID FLOW

www.elsevier.com/locate/ijhff

Natural convection cooling of rectangular and cylindrical containers

Wenxian Lin *, S.W. Armfield

Department of Mechanical and Mechatronic Engineering, The University of Sydney, NSW 2006, Australia

Received 3 September 1999; accepted 11 April 2000

Abstract

Scalings are obtained for the development of unsteady natural convection, both in rectangular and vertical circular containers, and are validated by comparison with results obtained using direct numerical simulation. It is found that the numerical results agree well with the scalings. Three main stages of flow evolution are identified and the differences at each of these stages between the rectangular and cylindrical geometries are quantified. It is shown that in the flow regimes considered there is a difference in thermal boundary layer thickness; that the horizontal intrusion layer has a uniform thickness for the rectangular flow, but increases towards the symmetry axis for the cylindrical flow; and that the rate of stratification is much faster for the cylindrical geometry.

Keywords: Scaling; Direct simulation; Unsteady natural convection

1. Introduction

Natural convection driven by buoyancy arising from an imposed horizontal density gradient is widely encountered in nature and in engineering situations, such as horizontal transport in water bodies, stratification processes in thermosyphon systems, crystal growth procedures and many others. In these applications, the buoyancy is unsteady, and the response of the system to changing conditions, especially to suddenly changing boundary conditions, is of fundamental interest.

The most studied form of this problem is the case of a rectangular cavity with differentially heated sidewalls. Batchelor (1954) first addressed the steady-state version of this problem. Since then, extensive experimental, numerical and analytical studies have been conducted on the topic. Much of this work is summarized in the reviews by Catton (1978) and Ostrach (1982). In spite of frequent occurrences of the unsteady case, however, the imposition of unsteady boundary conditions was evidently not considered in any detail until Patterson and Imberger (1980, hereafter referred to as simply P&I) discussed the case of instantaneous heating and cooling of the opposing sidewalls in a rectangular cavity. In that work, they addressed the problem of transient natural convection in a cavity of $A \leqslant 1$ with differentially heated end walls and carried out a scaling analysis to show that a number of initial flow types are possible, collapsing ultimately onto two basic types of steady flow, determined by the relative values of Ra, Pr and A which describe the flow. This flow model has since occupied the center stage of research into understanding natural convection in cavities and numerous investigations subsequently focused on diverse aspects of the model. Nicolette and Yang (1985) made a numerical and experimental investigation into two-dimensional transient natural convection of single-phase fluids inside a completely filled square enclosure with one vertical wall cooled and the other three walls insulated. Schladow et al. (1989) conducted a series of two- and three-dimensional numerical simulations of transient flow in a side-heated cavity and their simulations generally agree with the results of the scaling arguments of P&I. The numerical study by Hyun (1985a) on the effect of Pr on the heat-up of a stratified fluid in an enclosure revealed that the evolution of the flow and temperature fields are influenced by Pr. Patterson and Armfield (1990) conducted detailed experimental and numerical investigations into the presence of travelling wave instabilities on the vertical thermal boundary layers and horizontal intrusions, the existence of a rapid flow divergence in the region of the outflow of the intrusions, and the presence of cavity-scale oscillations caused by the interaction of the intrusion with the opposing vertical boundary layer. Furthermore, Armfield and Patterson (1991, 1992), Armfield and Janssen (1996) and Janssen and Armfield (1996) made in-depth studies on the wave and stability properties of the boundary layers in the cavities. The studies on unsteady natural convection in an enclosure until 1994 are well-documented in the review by Hyun (1994). Recently, Xin and Le Quéré (1995) investigated numerically chaotic natural convection in a differentially heated air-filled cavity with adiabatic horizontal walls while Brooker et al. (1997) conducted a non-parallel linear stability analysis of the vertical boundary layer in a differentially heated cavity.

* Corresponding author. Fax: +61-2-9351-7060.
E-mail address: lin@orr.mech.eng.usyd.edu.au (W. Lin).

0142-727X/01/$ - see front matter
PII: S0142-727X(00)00065-5

Notation

A	container aspect ratio, H/L
C_s	constant of proportionality, defined in (19)
C_u	constant, defined by (17)
g	acceleration due to gravity
H	container height
j	index denoting rectangular or cylindrical case
L	container half-width or radius
Nu	Nusselt number on sidewall
p	$p = P/(\rho U_0^2)$
P	pressure
Pr	Prandtl number, $Pr = \nu/\kappa$
Q_H	fluid flux through vertical thermal boundary layer
Ra	Rayleigh number, $Ra = g\beta H^3(T_w - T_a)/(\nu\kappa)$
t	time
T	temperature
T_a	fluid temperature in container
T_w	temperature imposed on sidewall
u	non-dimensionalized horizontal velocity component, $u = U/U_0$
$u_{x,c}$	non-dimensionalized velocity scale of horizontal intrusion layer at x
$\bar{u}$	non-dimensionalized mean velocity scale of horizontal intrusion layer moving from sidewall to symmetry axis, defined by (16)
U	horizontal velocity component
U_0	characteristic velocity, $U_0 = \kappa Ra^{1/2}/H$
v	non-dimensionalized vertical velocity component, $v = V/U_0$
v_{bs}	non-dimensionalized vertical velocity scale in vertical thermal boundary layer
V	vertical velocity component
x	non-dimensionalized horizontal coordinate, $x = X/H$
X	horizontal coordinate
y	non-dimensionalized vertical coordinate, $y = Y/H$
y_s	stratification height
Y	vertical coordinate

Greeks

β	thermal expansion coefficient
δ_{bs}	non-dimensionalized thickness scale of vertical thermal boundary layer
θ	$\theta = (T - T_a)/(T_w - T_a)$
κ	thermal diffusivity
ν	kinematic viscosity
ρ	density
τ	$\tau = t/(H/U_0)$
τ_{bs}	non-dimensionalized time scale for full growth of vertical thermal boundary layer
$\tau_{i,r}$	non-dimensional time scale of horizontal viscous intrusion layer for rectangular case
$\tau_{i,c}$	non-dimensional time scale of horizontal viscous intrusion layer for cylindrical case
τ_s	non-dimensional time scale of stratification development
$\tau_{s,f}$	non-dimensional time scale for full stratification
$\tau_{x,c}$	non-dimensional time scale of horizontal intrusion layer at x for cylindrical case
$\Delta_{i,r}$	non-dimensionalized thickness scale of horizontal viscous intrusion layer for rectangular case
$\Delta_{x,c}$	non-dimensionalized thickness scale of horizontal viscous intrusion layer at x
$\Delta\tau$	non-dimensionalized time step

The studies of the transient unsteady process of cooling down and stratifying a homogeneous fluid by natural convection in a vertical circular container are rare. Otis and Roessler (1987) conducted an experimental investigation into the development of stratification of gas in a cylindrical enclosure and provided experimental support for the existence of internal waves and revealed several time constants that characterize the process. Sakurai and Matsuda (1972) conducted a theoretical investigation into the transient process in an already stratified fluid and their analysis clearly revealed the core of the intricate physics involved in the transient adjustment process of a stratified fluid system in response to changes in thermal boundary conditions in a vertical circular container. This analysis was further modified and extended by Jischke and Doty (1975). Numerical investigation on this topic was addressed by Hyun et al. (1982), Hyun (1985b) and Hyun and Choi (1989) who obtained finite-difference numerical solutions of the complete time-dependent, Navier–Stokes equations describing the transient process of the Sakurai and Matsuda model. All these studies have focused on the situations in which, at the initial state, the fluid is already stratified. However, the transient evolving process from the initial state of non-stratification, e.g., a homogeneous fluid, to a finally stratified state possesses some characteristically different features and this transient process is of interest from the standpoint of both basic fluid dynamics and practical applications, as the production of a stratified fluid system of any strength is usually initialized using a homogeneous fluid. On this topic, only the experimental study mentioned above (Otis and Roessler, 1987) and numerical studies by Hyun (1984) and by Kwak et al. (1998) are found. In the study of Hyun (1984), the flow and temperature structures of the heat-up process of an initially homogeneous fluid in a cylinder with a linearly heated sidewall were elucidated using a finite-difference model. In the study of Kwak et al. (1998), a numerical study was conducted to investigate the transient natural convective cooling-down process of a fluid in a cylindrical container, with emphasis on the flow patterns when the maximum density temperature is experienced. Recently, a numerical investigation into the transient flow patterns of natural convection cooling in a vertical circular cylinder was carried out by Lin and Armfield (1999, hereafter referred to as simply L&A). In that study, the transient flow patterns are identified by the visualization of the transient evolving processes in the cylinder. The results show that vigorous flow activities concentrate mainly in the vertical thermal boundary layer along the sidewall and in the horizontal region which is the lower part of the domain where the cold intrusion flow is embedded. The transient flow patterns at the unsteady and quasi-steady stages were analyzed, including the activities of the travelling waves in the vertical thermal boundary layer on the sidewall and the cold intrusions in the horizontal region.

For the unsteady natural convection flow both in a rectangular container and in a vertical circular container, the flow developments are represented by three distinct stages, that is, the growth of the vertical thermal boundary layer on the sidewalls, the movement of the horizontal intrusion, and the stratification of fluid in the containers. P&I obtained the time, thickness and velocity scales characterizing the growth of the vertical thermal boundary layer on the sidewall, the time and thickness scales characterizing the movement of a horizontal intrusion layer and a time scale characterizing the full

stratification of fluid in a rectangular cavity with differentially heated sidewalls but no scales were obtained to characterize the rate of the stratification. These scalings were validated by experiments and numerical simulations for combinations of A, Pr and Ra. L&A obtained some scalings for the unsteady natural convection flow in a vertical circular container with cooled sidewall, but a more comprehensive scaling analysis is still needed. We were therefore motivated to conduct the current study, with the additional purpose of elucidating the quantitative differences between the unsteady natural convection cooling of a homogeneous fluid in a rectangular container and in a vertical circular container. In Section 2, a range of scalings will be derived and the numerical method described. The scalings will be validated in Section 3 by comparison with numerical results obtained with $Pr = 7$ and $A = 1$. Section 4 contains the conclusions.

2. Scalings and numerical method

2.1. Governing equations

Under consideration is the unsteady natural convection flow both in a rectangular container with a height of H and a width of $2L$ and in a vertical circular container with the same height and a radius of L. The top and bottom walls of the containers are thermally insulated. Initially the fluids in the containers are at rest and at temperature T_a, and at $t = 0$ their vertical sidewalls are cooled impulsively to T_w and this temperature is maintained thereafter. It is assumed that the flow in the rectangular container is symmetric about the center line and two-dimensional while the flow in the vertical circular container is assumed to be axisymmetric. Therefore, the computational domain sketched in Fig. 1 is appropriate, where a Cartesian and a cylindrical coordinate system are used, respectively, for flows in the rectangular and in the vertical circular container. For brevity, the flows in these two containers are referred to as simply the rectangular and cylindrical case, respectively.

The flow is described by the Navier–Stokes equations and the temperature equation, with the Boussinesq assumption allowing their incompressible forms to be used. The governing equations are written in non-dimensional form as follows:

$$\frac{1}{x^j}\frac{\partial(x^j u)}{\partial x}+\frac{\partial v}{\partial y}=0, \tag{1}$$

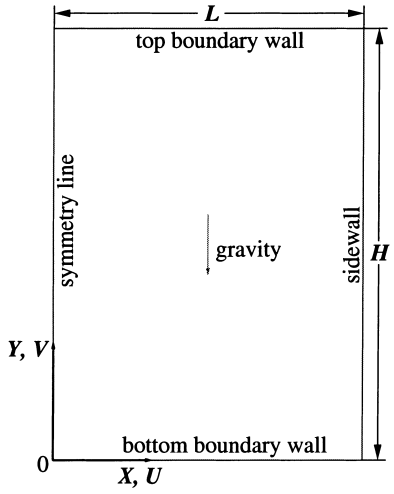

Fig. 1. Computational domain and coordinate system.

$$\frac{\partial u}{\partial \tau}+\frac{1}{x^j}\frac{\partial(x^j uu)}{\partial x}+\frac{\partial(vu)}{\partial y} = -\frac{\partial p}{\partial x}+\frac{Pr}{Ra^{1/2}}\left\{\frac{\partial}{\partial x}\left[\frac{1}{x^j}\frac{\partial(x^j u)}{\partial x}\right]+\frac{\partial^2 u}{\partial y^2}\right\}, \tag{2}$$

$$\frac{\partial v}{\partial \tau}+\frac{1}{x^j}\frac{\partial(x^j uv)}{\partial x}+\frac{\partial(vv)}{\partial y} = -\frac{\partial p}{\partial y}+\frac{Pr}{Ra^{1/2}}\left[\frac{1}{x^j}\frac{\partial}{\partial x}\left(x^j\frac{\partial v}{\partial x}\right)+\frac{\partial^2 v}{\partial y^2}\right]+Pr\theta, \tag{3}$$

$$\frac{\partial \theta}{\partial \tau}+\frac{1}{x^j}\frac{\partial(x^j u\theta)}{\partial x}+\frac{\partial(v\theta)}{\partial y}=\frac{1}{Ra^{1/2}}\left[\frac{1}{x^j}\frac{\partial}{\partial x}\left(x^j\frac{\partial \theta}{\partial x}\right)+\frac{\partial^2\theta}{\partial y^2}\right], \tag{4}$$

where $j = 0$ and 1 denote the rectangular and cylindrical cases, respectively.

Non-dimensional quantities are obtained as follows:

$$x=\frac{X}{H},\quad y=\frac{Y}{H},\quad u=\frac{U}{U_0},\quad v=\frac{V}{U_0},$$
$$\tau=\frac{t}{(H/U_0)},\quad p=\frac{P}{\rho U_0^2},\quad \theta=\frac{T-T_a}{T_w-T_a}, \tag{5}$$

where $U_0 = \kappa Ra^{1/2}/H$, the velocity scale of the thermal boundary layer obtained by P&I, is used.

The associated initial and boundary conditions are

$$u = v = 0,\quad \theta = 0 \text{ at all } x, y \text{ and } \tau < 0, \tag{6}$$

and

$$\begin{aligned} &u = v = 0,\quad \partial\theta/\partial y = 0 \text{ on } y = 0, 1,\\ &u = 0,\quad \partial v/\partial x = \partial\theta/\partial x = 0 \text{ on } x = 0,\\ &u = v = 0,\quad \theta = -1 \text{ on } x = 1/A \text{ for } \tau \geqslant 0. \end{aligned} \tag{7}$$

2.2. Scaling analysis

2.2.1. Growth of the vertical thermal boundary layer

In the vertical boundary layer regions on the sidewalls, the non-dimensionalized boundary layer thickness, vertical velocity and time scales are δ_{bs}, v_{bs} and τ_{bs}, respectively, while the non-dimensionalized height scale is 1. In the following analysis, it is assumed that $\delta_{bs} \ll 1$ which requires $Ra > Pr^2$, as shown by P&I.

Heat is initially conducted out of the fluid and into the sidewall, resulting in a vertical thermal boundary layer of thickness $O(\delta_b(\tau))$, where, from (4)

$$\delta_b(\tau) \sim Ra^{-1/4}\tau^{1/2} \tag{8}$$

for the rectangular case. Correspondingly, the Nusselt number, Nu, on the sidewall has the following scaling with Ra and τ:

$$Nu=\int_0^1 \frac{\partial\theta}{\partial x}\,dy \sim \delta_b(\tau)^{-1} \sim Ra^{1/4}\tau^{-1/2}, \tag{9}$$

which gives the total non-dimensional conductive heat transfer from the fluid to the cooled wall.

When the vertical thermal boundary layer is fully developed, the following scalings were obtained by P&I:

$$\tau_{bs} \sim 1,\quad v_{bs} \sim 1,\quad \delta_{bs} \sim Ra^{-1/4}. \tag{10}$$

The scalings (8)–(10) are also valid for the cylindrical case if the assumption of $Ra > Pr^2$ is still satisfied.

2.2.2. Passage of the horizontal viscous intrusion layer

After the establishment of the vertical thermal boundary layer on the sidewall, a horizontal intrusion layer begins to

form and move towards the symmetry axis on the bottom floor of the containers.

In the rectangular case, it was shown by P&I that for $Pr^4A^{-4} < Ra < Pr^{16}A^{-12}$ the intrusion is viscous and the non-dimensionalized time scale $\tau_{i,\mathrm{r}}$ for the intrusion to reach the symmetry axis is scaled by A and Ra as follows:

$$\tau_{i,\mathrm{r}} \sim A^{-5/4} Ra^{1/16}, \tag{11}$$

at which time the intrusion grows to a non-dimensionalized thickness $\Delta_{i,\mathrm{r}}$, where

$$\Delta_{i,\mathrm{r}} \sim A^{-1/4} Ra^{-3/16}. \tag{12}$$

In the cylindrical case, the constant flux intrusion layer is also driven by a buoyancy-induced horizontal pressure gradient of $\mathrm{O}(\Delta_{x,\mathrm{c}} Pr\theta/u_{x,\mathrm{c}}\tau_{x,\mathrm{c}})$, from (3), where $\Delta_{x,\mathrm{c}}$ and $u_{x,\mathrm{c}}$ are the non-dimensionalized thickness and velocity of the intrusion layer at horizontal location x and at a non-dimensionalized time scale $\tau_{x,\mathrm{c}}$. A viscous-pressure balance, from (2), gives

$$\frac{Pr}{Ra^{1/2}} \frac{u_{x,\mathrm{c}}}{\Delta_{x,\mathrm{c}}^2} \sim \frac{p}{u_{x,\mathrm{c}}\tau_{x,\mathrm{c}}} \sim \frac{\Delta_{x,\mathrm{c}} Pr\theta}{u_{x,\mathrm{c}}\tau_{x,\mathrm{c}}}. \tag{13}$$

which results in

$$\Delta_{x,\mathrm{c}}^5 \sim \frac{Q_H^2 \tau_{x,\mathrm{c}}}{x^2 Ra^{1/2}} \tag{14}$$

as $\mathrm{O}(\theta) = 1$, where $Q_H \sim v_{bs}\delta_{bs}/A \sim Ra^{-1/4}A^{-1} \sim x\Delta_{x,\mathrm{c}}u_{x,\mathrm{c}}$ is the flux of fluid discharged from the vertical thermal boundary layer. As $\tau_{x,\mathrm{c}} \sim (A^{-1} - x)/u_{x,\mathrm{c}}$, the thickness of the intrusion layer at x is scaled with A and Ra as follows:

$$\Delta_{x,\mathrm{c}} \sim \frac{(A^{-1}x^{-1} - 1)^{1/4}}{A^{1/4} Ra^{3/16}}. \tag{15}$$

The mean velocity scale $\bar{u}$ of the horizontal intrusion layer moving from the sidewall to the symmetry axis is

$$\bar{u} \sim A \int_0^{A^{-1}} u_{x,\mathrm{c}}\,\mathrm{d}x \sim A \int_0^{A^{-1}} \frac{Q_H}{x\Delta_{x,\mathrm{c}}}\,\mathrm{d}x \sim Q_H A^{1/4} Ra^{3/16} C_{\mathrm{u}} \tag{16}$$

and

$$C_{\mathrm{u}} = A \int_0^{A^{-1}} x^{-1} \left(\frac{1}{Ax} - 1\right)^{-1/4} \mathrm{d}x \cong 3.5 \tag{17}$$

for $\delta_{\mathrm{bs}} \ll 1$ which requires that $Ra > Pr^2$.

Therefore, from (16), a non-dimensionalized time scale $\tau_{i,\mathrm{c}}$ for the horizontal intrusion layer to arrive at the symmetry axis can be obtained for the cylindrical case, that is,

$$\tau_{i,\mathrm{c}} \sim \frac{A^{-1}}{\bar{u}} \sim A^{-1/4} Ra^{1/16}. \tag{18}$$

It is apparent that Nu should be constant for both the rectangular and cylindrical cases during the passage of the horizontal viscous intrusion layer towards the symmetry axis on the container floor as there is no change in the boundary layer during that time.

2.2.3. Stratification of the core

After the arrival of the horizontal viscous intrusion at the symmetry axis, the containers begin to be filled with stratified fluid. L&A obtained scalings for the rate of stratification and the time to full stratification for the cylindrical case, that is, at a non-dimensionalized time τ the stratification height $y_{\mathrm{s}}(\tau)$ is

$$y_{\mathrm{s}}(\tau) \sim 1 - \left(1 - \frac{C_s A\tau}{Ra^{1/4}}\right)^4, \tag{19}$$

where C_{s} is a constant of proportionality. The container will be fully stratified when $y_{\mathrm{s}}(\tau) = 1$, giving a non-dimensionalized time scale for the full stratification $\tau_{\mathrm{s,f}}$ as follows:

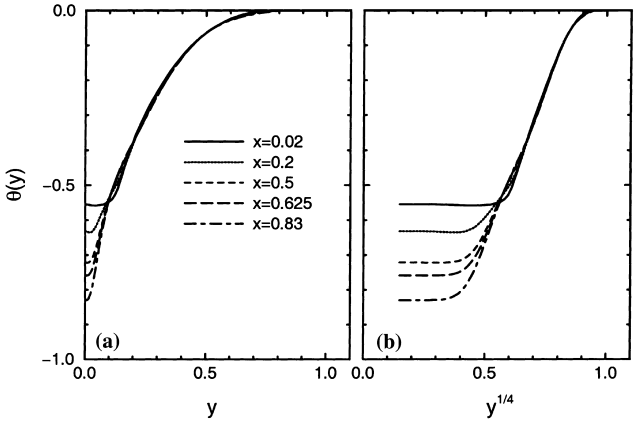

Fig. 2. Vertical profiles of temperature at location $x = 0.02, 0.2, 0.5, 0.625$ and 0.83 at $\tau = 30$ for $Ra = 1 \times 10^8$, $Pr = 7$ and $A = 1$ in the rectangular case: (a) θ plotted against y; (b) θ plotted against $y^{1/4}$.

$$\tau_{\mathrm{s,f}} \sim \frac{Ra^{1/4}}{C_s A}. \tag{20}$$

The scalings (19) and (20) may also be obtained for the rectangular case. P&I obtained (20) for the full stratification in the rectangular case, but obtained no scaling for the rate of stratification.

To obtain a scaling for Nu during the stratification of the core, it is necessary to scale $\theta(y)$, the temperature of the stratified layer within the container. Fig. 2(a) shows vertical profiles of temperature at locations $x = 0.02, 0.2, 0.5, 0.625$ and 0.83 at $\tau = 30$ for $Ra = 1 \times 10^8$, $Pr = 7$ and $A = 1$ in the rectangular case. It is observed that away from the wall and the small y region, the values all fall on a single curve, showing that over most of the fluid there is little x variation. In Fig. 2(b), temperature is plotted against $y^{1/4}$ showing that over most of the stratified region of the container

$$\theta(y) \sim y^{1/4}. \tag{21}$$

To obtain the Nusselt number at the wall during stratification it is necessary to separate the stratified and non-stratified sections, giving

$$Nu = \int_0^{y_{\mathrm{s}}} \frac{1 - \theta(y)}{\delta_{\mathrm{bs}}(y_{\mathrm{s}})}\,\mathrm{d}y + \int_{y_{\mathrm{s}}}^1 \frac{1}{\delta_{\mathrm{bs}}(y_{\mathrm{s}})}\,\mathrm{d}y \sim Ra^{1/4}(1 - 0.8y_{\mathrm{s}}^{5/4}) \sim Ra^{1/4} f(\tau Ra^{-1/4}). \tag{22}$$

The scalings (21) and (22) are also obtained for the cylindrical cases.

2.3. Numerical method

2.3.1. Discretization and time integration

Because of the large variation in length scales it is necessary to use a mesh that concentrates points in the boundary layer and is relatively coarse in the interior. The meshes are constructed using a stretched grid. The basic mesh uses 95×95 grid points, which are distributed symmetrically with respect to the domain half-width and half-height. The nearest grid-point is located 0.0005 of the domain width from the wall or the symmetry axis. Subsequently, the mesh expands at a rate of 10% up to $x = 0.1$ or $y = 0.1$. After that, the mesh size expansion rate decreases until it reaches 0, resulting in a constant coarse mesh in the interior of the domain. The basic time step used for the calculation is $\Delta\tau = 5 \times 10^{-5}$.

The equations are discretized on a non-staggered mesh using finite volumes, with standard second-order central differences used for the viscous, the pressure gradient and divergence terms. The QUICK third-order upwind scheme (Leonard, 1979) is used for the advective terms. The momentum and temperature equations are solved using an ADI scheme. The second-order Adams–Bashforth scheme and Crank–Nicholson scheme are used for the time integration of the advective terms and the diffusive terms, respectively. To enforce continuity, the pressure correction method is used to construct a Poisson's equation which is solved using the preconditioned GMRES method (Armfield, 1991, 1994; Armfield and Street, 1999) and the code has been previously used for the simulation of buoyancy dominated flows (Patterson and Armfield, 1990; Armfield and Patterson, 1992; Armfield and Debler, 1993; Armfield and Janssen, 1996; Lin and Armfield, 1999, 2000a,b).

2.3.2. Grid independence

To test the grid independence of the scheme, the solution has been obtained on the basic mesh of 95×95 defined above, which is the mesh used in this study, and on two additional meshes, with the following parameters. The first mesh has 2.5 times the size at the wall and at the symmetry axis, the same grid expansion factor, and two times the time step of the basic mesh. This gives a grid of 77×77 with approximately the same grid spacing in the core. The second mesh has five times the size at the wall and at the symmetry axis, the same grid expansion factor, and five times the time step of the basic mesh. This gives a grid of 59×59. Figs. 3(a)–(d) show, respectively, the temperature and vertical velocity profiles as a function of horizontal distance at mid-height in the thermal boundary layer for both the rectangular and cylindrical cases for $A = 1$, $Ra = 1 \times 10^9$ and $Pr = 7$ at $\tau = 0.2$. It is seen that the variation between the three representations is very small, indicating that the basic mesh of 95×95 is free of grid- and time-step-dependent errors.

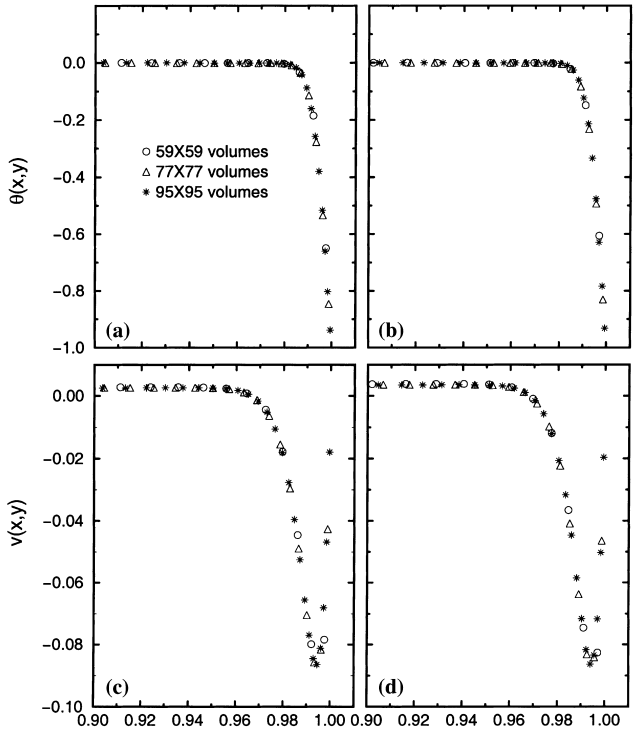

Fig. 3. Comparison of the results from the 95×95 basic mesh, 77×77 mesh and 59×59 mesh for the horizontal profiles of temperature and vertical velocity at mid-height of the container at time $\tau = 0.2$ for both the rectangular case and in the cylindrical case: (a) temperature in the rectangular case; (b) temperature in the cylindrical case; (c) vertical velocity in the rectangular case; (d) vertical velocity in the cylindrical case.

3. Validation of scalings by numerical simulations

To validate the scalings obtained above and to quantify the differences between the rectangular and cylindrical cases, direct numerical simulations of unsteady natural convection cooling of a homogeneous fluid for both the rectangular and cylindrical geometries were conducted for $Ra = 1 \times 10^6$, 1×10^7, 5×10^7, 1×10^8, 5×10^8 and 1×10^9. The 95×95 mesh with $Pr = 7$, $A = 1$, $\Delta\tau = 5 \times 10^{-5}$ and the divergence–convergence criterion of 1×10^{-4} are used in all the numerical simulations.

3.1. Growth of the vertical thermal boundary-layer

In Fig. 4, the time series of the non-dimensionalized thickness $\delta_{bs}(\tau)$ at $y = 0.5$, the Nusselt number Nu on the sidewall and the maximum vertical velocity $v_{bs}(\tau)$ at $y = 0.5$ of the vertical thermal boundary layer on the sidewall are shown for the six Rayleigh numbers aforementioned for both the rectangular and cylindrical cases. The boundary layer grows after the initiation of cooling, reaching a maximum thickness at this height at $\tau = 1.5$, then drops slightly to achieve a steady state by $\tau = 2.0$. Similarly, the velocity magnitude grows ini-

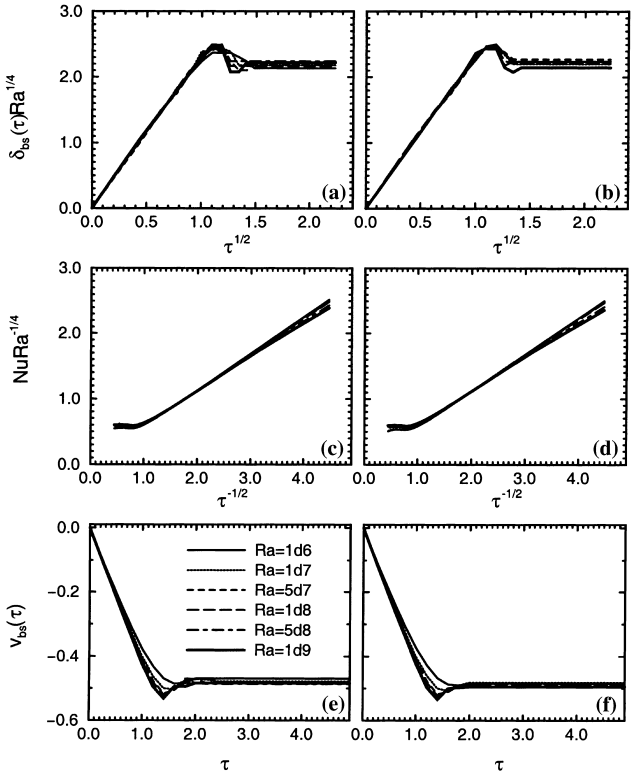

Fig. 4. $\delta_{bs}(\tau)Ra^{1/4}$ plotted against $\tau^{1/2}$ for $Ra = 1 \times 10^6$, 1×10^7, 5×10^7, 1×10^8, 5×10^8 and 1×10^9 up to $\tau = 5$ in: (a) the rectangular case; (b) the cylindrical case. $NuRa^{-1/4}$ plotted against $\tau^{-1/2}$ in: (c) the rectangular case; (d) the cylindrical case. $v_{bs}(\tau)$ plotted against τ in: (e) the rectangular case; (f) the cylindrical case.

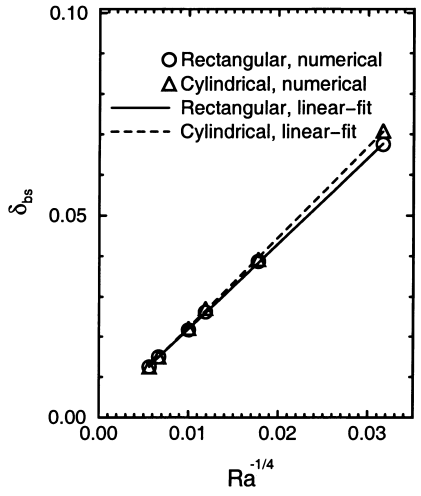

Fig. 5. δ_{bs} plotted against $Ra^{-1/4}$ for six Rayleigh numbers for both the rectangular and cylindrical cases.

tially reaching a maximum at $\tau = 1.5$ and full development at $\tau = 2.0$. The $Ra^{-1/4}\tau^{1/2}$ scaling for δ_{bs} and $Ra^{1/4}\tau^{-1/2}$ scaling for Nu collapse all the Ra results onto single curves for this stage of the flow, with the relation for the growth phase being linear, indicating that these are the correct scalings for these quantities. The time scale for full development of the boundary layer at this height, τ_{bs}, is approximately 2.0 for all the Rayleigh numbers considered.

The maximum thicknesses of the vertical thermal boundary layers for the six Rayleigh numbers at full development are shown in Fig. 5 for the two cases. It is seen that δ_{bs} has a linear relation with $Ra^{-1/4}$, that is,

$$\delta_{bs} = 2.114\,Ra^{-1/4} \tag{23}$$

for the rectangular case and

$$\delta_{bs} = 2.235\,Ra^{-1/4} \tag{24}$$

for the cylindrical case. These relations confirm the scaling thickness given in (10). From these relations, it is also seen that the vertical thermal boundary layer becomes slightly thicker for the cylindrical case than for the rectangular case.

3.2. Passage of the horizontal viscous intrusion layer

After the boundary is fully developed, the intrusion generated at the downstream end of the boundary layer travels across the domain from the cooled wall to the symmetry axis. In Figs. 6–9, the transient temperature and stream function contours at $\tau = 1, 2, 3, 4$ and 5 are shown for $Ra = 1 \times 10^6$, 1×10^7, 1×10^8 and 1×10^9 for both the rectangular and cylindrical cases. Some features can been seen immediately from these figures. One is that the thickness of the horizontal viscous intrusions for the rectangular case are almost constant as the intrusions approach the symmetry axis, whereas for the cylindrical case they increase as they move towards the symmetry axis. The second feature is that the thicknesses of the intrusion layers becomes smaller when Ra increases for both the cases. Another is that the non-dimensional times for the intrusion layer to arrive at the symmetry axis become longer when Ra increases. All these observations agree qualitatively with the scalings given in (11), (12), (15) and (18).

In Fig. 10, the times $\tau_{i,r}$ and $\tau_{i,c}$ for the horizontal intrusion layers to arrive at the symmetry axis are plotted against $Ra^{1/16}$, where $\tau_{i,r}$ and $\tau_{i,c}$ are defined as the time when the temperature

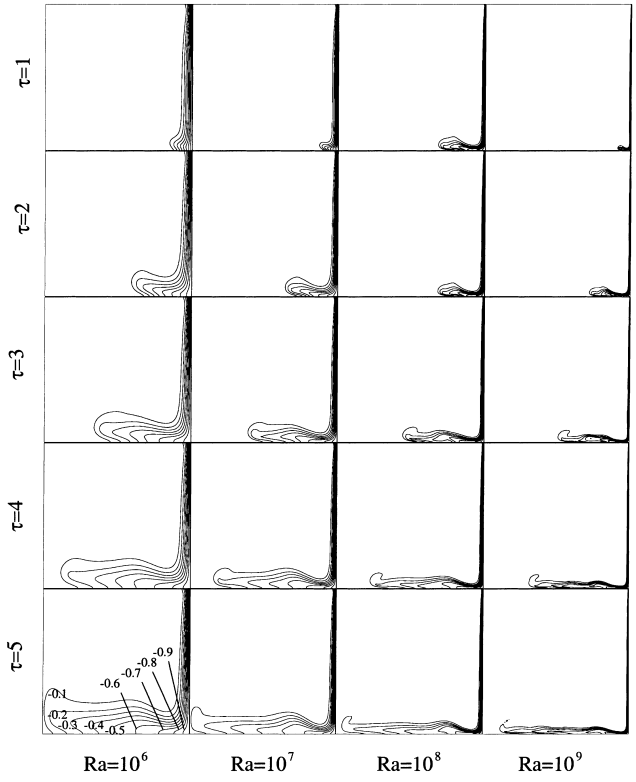

Fig. 6. Temperature contours in the computational domain for $Ra = 10^6$, 10^7, 10^8 and 10^9 at $\tau = 1, 2, 3, 4,$ and 5 in the rectangular case.

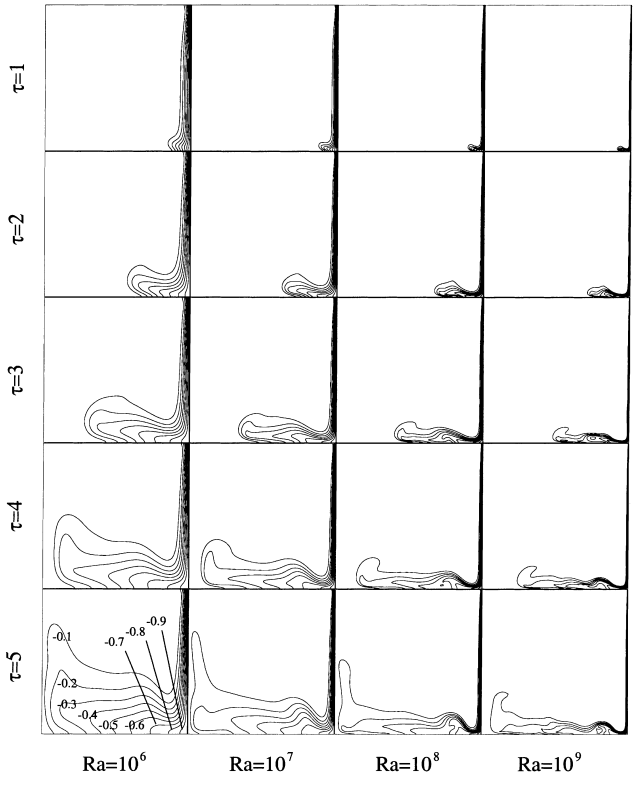

Fig. 7. Temperature contours in the computational domain for $Ra = 10^6$, 10^7, 10^8 and 10^9 at $\tau = 1$, 2, 3, 4, and 5 in the cylindrical case.

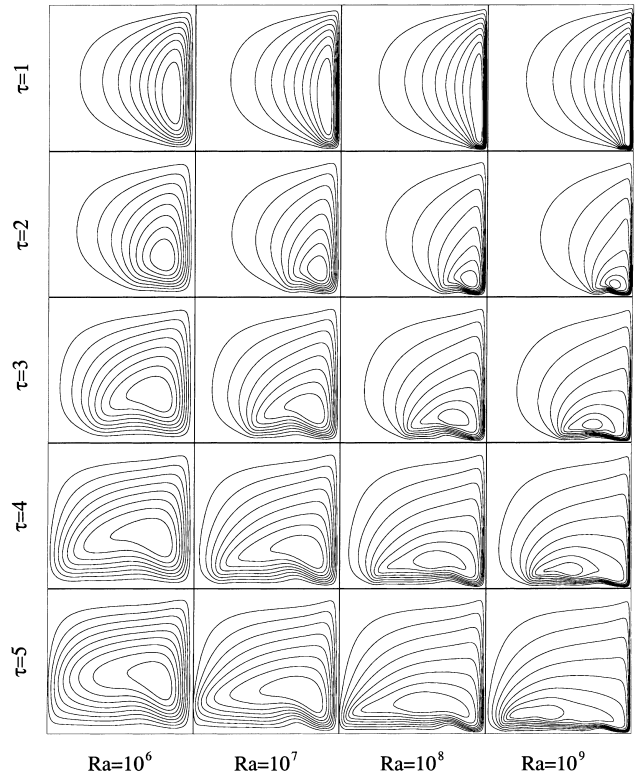

Fig. 8. Stream function contours in the computational domain for $Ra = 10^6$, 10^7, 10^8 and 10^9 at $\tau = 1$, 2, 3, 4, and 5 in the rectangular case.

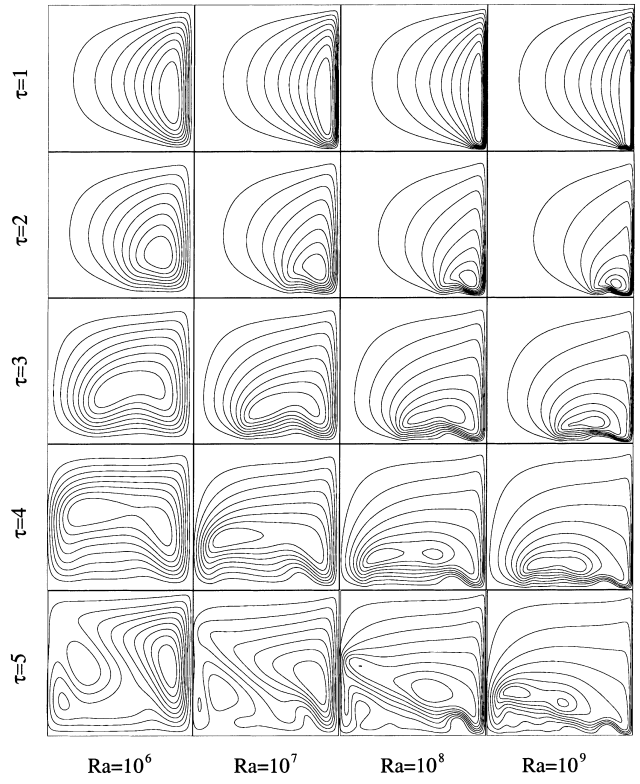

Fig. 9. Stream function contours in the computational domain for $Ra = 10^6$, 10^7, 10^8 and 10^9 at $\tau = 1$, 2, 3, 4, and 5 in the cylindrical case.

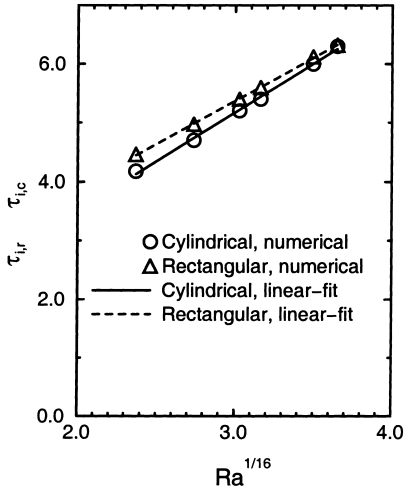

Fig. 10. $\tau_{i,\mathrm{r}}$ and $\tau_{i,\mathrm{c}}$ plotted against $Ra^{1/16}$ for $Ra = 1 \times 10^6$, 1×10^7, 5×10^7, 1×10^8, 5×10^8 and 10^9 in the rectangular and cylindrical cases.

at the first grid near the symmetry axis in the computational domain becomes -0.01 for the first time. The resulting linear relations between $\tau_{i,\mathrm{r}}$ and $Ra^{1/16}$ and between $\tau_{i,\mathrm{c}}$ and $Ra^{1/16}$ are well predicted by the following expressions:

$$\tau_{i,\mathrm{r}} = 0.188 + 1.662\,Ra^{1/16} \tag{25}$$

for the rectangular case and

$$\tau_{i,\mathrm{c}} = 0.962 + 1.469\,Ra^{1/16} \tag{26}$$

for the cylindrical case. These correlations confirm quantitatively the scalings (11) and (18). For all the Rayleigh numbers considered, the horizontal intrusion layer in the cylindrical case takes a slightly shorter time than that in the rectangular case to arrive at the symmetry axis although this quantitative difference becomes smaller when Ra increases.

The qualitative observation that the thickness of the horizontal viscous intrusion layers, which is defined as the thickness when the edge of the intrusion layer is at $\theta = -0.01$, are almost uniform for the rectangular case as the intrusions approach the symmetry axis is also quantitatively confirmed by the results shown in Fig. 11 where $\Delta_{i,\mathrm{r}} Ra^{3/16}$ is plotted against x

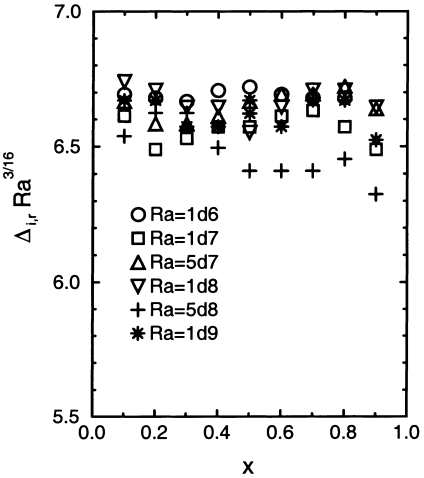

Fig. 11. $\Delta_{i,\mathrm{r}} Ra^{3/16}$ plotted against x for $Ra = 1 \times 10^6$, 1×10^7, 5×10^7, 1×10^8, 5×10^8 and 10^9 in the rectangular case.

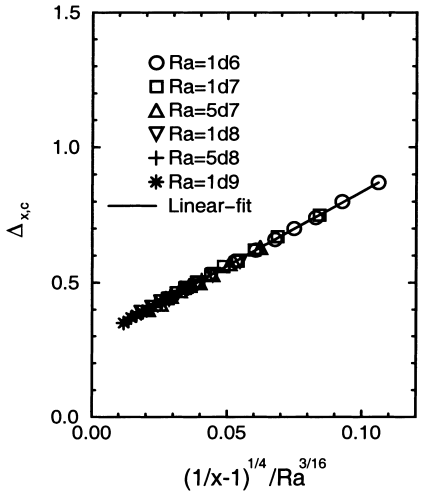

Fig. 12. $\Delta_{x,c}$ plotted against $(1/x-1)^{1/4}Ra^{-3/16}$ for $Ra = 1\times10^6$, 1×10^7, 5×10^7, 1×10^8, 5×10^8 and 10^9 in the cylindrical case.

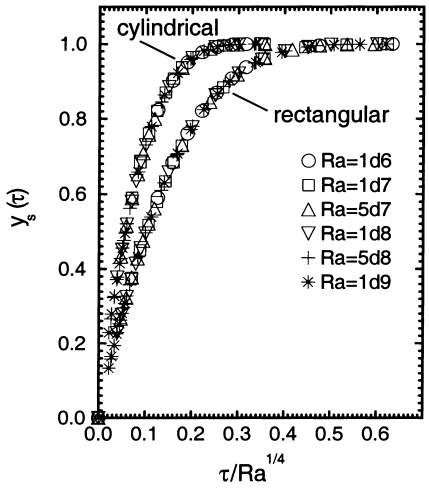

Fig. 13. $y_s(\tau)$ plotted against $\tau Ra^{-1/4}$ for $Ra = 1\times10^6$, 1×10^7, 5×10^7, 1×10^8, 5×10^8 and 10^9 in the rectangular and cylindrical cases.

for six Rayleigh numbers for the rectangular case. The correlation is found to have the following expression:

$$\Delta_{i,r} = 6.642Ra^{-3/16} \tag{27}$$

confirming the scaling (12).

The thickness of the horizontal viscous intrusions as they approach the symmetry axis for the cylindrical case is presented in Fig. 12 where $\Delta_{x,c}$ is plotted against $(x^{-1}-1)^{1/4}/Ra^{3/16}$ for six Rayleigh numbers for the cylindrical case. The scaling (15) is confirmed by the numerical result and the linear correlation between $\Delta_{x,c}$ and $(x^{-1}-1)^{1/4}/Ra^{3/16}$ is as follows:

$$\Delta_{x,c} = 0.287 + 5.495\frac{(x^{-1}-1)^{1/4}}{Ra^{3/16}}. \tag{28}$$

From Fig. 4 above, it is observed that the Nusselt numbers on the sidewall during the passage of the horizontal viscous intrusion layer are constant for all the numerical simulations, confirming the scaling result shown above.

3.3. Stratification of the core

After the intrusion has reached the symmetry axis, the domain begins to fill with stratified fluid. During this period, the domain core is composed of a lower region containing stratified fluid and an upper region where the fluid is at the initial ambient temperature. The region of stratified fluid gradually rises until the domain is fully stratified.

In Fig. 13, the filled height $y_s(\tau)$, which is defined as the height where the temperature of the fluid is at $\theta = -0.01$ and at $x = 0.5$, is plotted against $\tau/Ra^{1/4}$ for six Rayleigh numbers for both the rectangular and cylindrical cases. The numerical results shown in this figure confirm the scaling (19). It is also observed that the rate of stratification in the cylindrical case is much faster than that in the rectangular case, as quantitatively shown in Fig. 14, where the time for full stratification τ_s is plotted against $Ra^{1/4}$ for six Rayleigh numbers for both the cases. The numerical results shown in Fig. 14 give the following correlations between τ_s and $Ra^{1/4}$, that is, for the rectangular case:

$$\tau_s = 0.639Ra^{1/4}, \tag{29}$$

which gives $C_s = 1.565$ as defined in the scalings (19) and (20), and for the cylindrical case

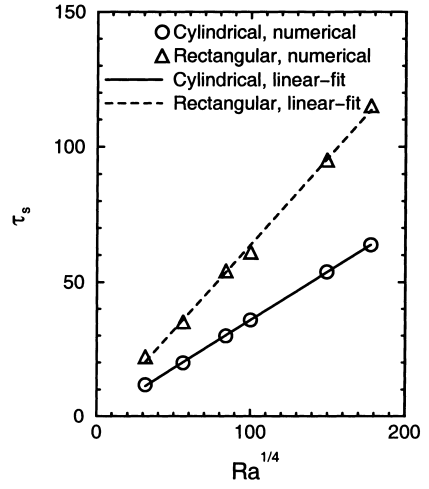

Fig. 14. τ_s plotted against $Ra^{1/4}$ for $Ra = 1\times10^6$, 1×10^7, 5×10^7, 1×10^8, 5×10^8 and 10^9 in the rectangular and cylindrical cases.

$$\tau_s = 0.359Ra^{1/4}, \tag{30}$$

which gives $C_s = 2.786$, further confirming the scalings (19) and (20).

In Fig. 15, $NuRa^{-1/4}$, where Nu is the Nusselt number on the sidewall during the stratification of the core, is plotted against $\tau Ra^{-1/4}$ for six Rayleigh numbers for both the rectangular and cylindrical cases. It is observed that all the data collapse onto a single curve, confirming the scaling (22).

4. Conclusions

A scaling analysis for unsteady natural convection in a rectangular container and in a vertical circular container has been conducted. For the rectangular case, most of the scalings had been previously obtained by P&I while the scaling for the rate of stratification and the scalings for the Nusselt number on the sidewall were obtained in this study. For the cylindrical case, the corresponding scalings for the horizontal viscous intrusions were obtained in the present study while the scalings for the rate of stratification and time to full stratification were

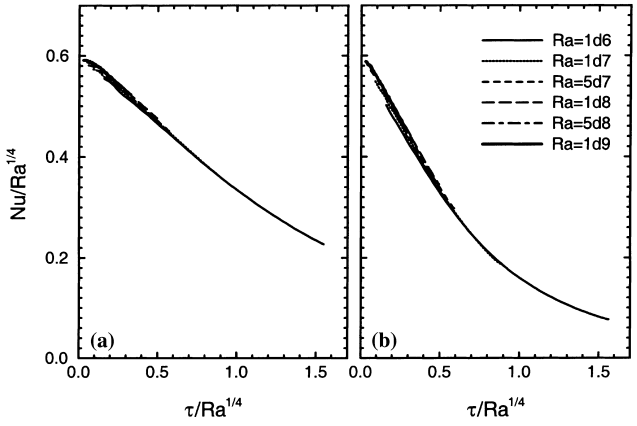

Fig. 15. $NuRa^{-1/4}$ plotted against $\tau Ra^{-1/4}$ for $Ra = 1 \times 10^6$, 1×10^7, 5×10^7, 1×10^8, 5×10^8 and 10^9 during the stratification of the core (from $\tau = 5$) in: (a) the rectangular case; (b) the cylindrical case.

previously obtained by L&A. All scalings have been validated by direct numerical simulation of the unsteady natural convection cooling of a homogeneous fluid for both the rectangular and the cylindrical cases. The differences between the rectangular and cylindrical flows at three stages in the development of full stratification have been quantified using the simulation results. The three stages are: the growth of the vertical thermal boundary layer on the sidewalls; the passage of the horizontal viscous intrusions; the stratification of the core. The most significant differences between the two cases are that for $A = 1$, $Pr = 7$, and $1 \times 10^6 \leqslant Ra \leqslant 1 \times 10^9$; the vertical thermal boundary layer is slightly thicker for the cylindrical case than for the rectangular case; the thickness of the horizontal viscous intrusion is almost uniform for the rectangular case whereas it increases gradually when the intrusion approaches the symmetry axis for the cylindrical case; the intrusions in the cylindrical case takes a slightly shorter time than that in the rectangular case to arrive at the symmetry axis although this quantitative difference becomes smaller when Ra increases; the rate of stratification of fluid in the cylindrical case is much faster than that in the rectangular case, with the difference increasing with Ra.

The differences between the rectangular and cylindrical cases can all be qualitatively related to the reduction in size of the volume element as the radius reduces for the cylindrical case. For both cases, the heat transfer to the sidewall is approximately the same with the reduction in the size of the volume element requiring the cylindrical boundary layer be slightly thicker than the rectangular boundary layer to transport the same heat and volume flux. Similarly, the volume flux for both intrusions is approximately equal requiring the cylindrical intrusion to thicken as the size of the volume element reduces. Finally, the filling rate will be determined by the ratio of the volume flux through the boundary layer to the volume of the cylinder and rectangular cavity leading to the more rapid filling for the cylindrical case. This effect also produces the more rapid reduction in Nu for the cylindrical case during the stratification stage.

Acknowledgements

We are very grateful for the reviewers' comments which helped us to clarity some important points. We also thank Prof. J.C. Patterson for his helpful discussion. The financial support of an AusAID Scholarship and from the National Natural Science Foundation and Yunnan Province of P.R. China to W. Lin is gratefully acknowledged.

References

Armfield, S.W., 1991. Finite difference solutions of the Navier–Stokes equations on staggered and non-staggered grids. Comput. Fluids 20, 1–17.

Armfield, S.W., 1994. Ellipticity, accuracy, and convergence of the discrete Navier–Stokes equations. J. Comput. Phys. 114, 176–184.

Armfield, S.W., Debler, W., 1993. Purging of density stabilized basins. Int. J. Heat Mass Transfer 36, 519–530.

Armfield, S.W., Janssen, R., 1996. A direct boundary-layer stability analysis of steady-state cavity convection flow. Int. J. Heat Fluid Flow 17, 539–546.

Armfield, S.W., Patterson, J.C., 1991. Direct simulation of wave interactions in unsteady natural convection in a cavity. Int. J. Heat Mass Transfer 34, 929–940.

Armfield, S.W., Patterson, J.C., 1992. Wave properties of natural-convection boundary layers. J. Fluid Mech. 239, 195–211.

Armfield, S.W., Street, R., 1999. The fractional-step method for the Navier–Stokes equations on staggered grids the accuracy of three variations. J. Comput. Phys. 153, 660–665.

Batchelor, G.K., 1954. Heat transfer by free convection across a closed cavity between vertical boundaries at different temperature. Q. J. Appl. Math. 12, 209–233.

Brooker, A.M.H., Patterson, J.C., Armfield, S.W., 1997. Non-parallel linear stability analysis of the vertical boundary layer in a differentially heated cavity. J. Fluid Mech. 352, 265–281.

Catton, I., 1978. Natural convection in enclosures. In: Proceedings of the Sixth International Heat Transfer Conference, Washington, DC.

Hyun, J.M., 1984. Transient process of thermally stratifying an initially homogeneous fluid in an enclosure. Int. J. Heat Mass Transfer 27, 1936–1938.

Hyun, J.M., 1985a. Effect of the Prandtl number on heat-up of a stratified fluid in a enclosure. ASME J. Heat Transfer 107, 982–984.

Hyun, J.M., 1985b. Transient buoyant convection of a contained fluid driven by the changes in the boundary temperatures. ASME J. Appl. Mech. 52, 193–198.

Hyun, J.M., 1994. Unsteady bouyant convection in an enclosure. Adv. Heat Transfer 24, 277–320.

Hyun, J.M., Choi, H.K., 1989. Transient cool down of a gas in a closed container. J. Thermophys. Heat Transfer 3, 441–446.

Hyun, J.M., Fowlis, W.W., Warn-Varnas, A., 1982. Numerical solutions for the spin-up of a stratified fluid. J. Fluid Mech. 117, 71–90.

Janssen, R., Armfield, S.W., 1996. Stability properties of the vertical boundary layers in differentially heated cavities. Int. J. Heat Fluid Flow 17, 547–556.

Jischke, M.C., Doty, R.T., 1975. Linearized buoyant motion in a closed container. J. Fluid Mech. 71, 729–754.

Kwak, H.S, Kuwahara, K., Hyun, J.M., 1998. Convective cool-down of a contained fluid through its maximum density temperature. Int. J. Heat Mass Transfer 41, 323–333.

Leonard, B.P., 1979. A stable and accurate convective modeling procedure based on quadratic upstream interpolation. Comp. Meth. Appl. Mech. Eng. 19, 59–98.

Lin, W., Armfield, S.W., 1999. Direct simulation of natural convection in a vertical circular cylinder. Int. J. Heat Mass Transfer 42, 4117–4130.

Lin, W., Armfield, S.W., 2000a. Direct simulation of weak axisymmetric fountains in a homogeneous fluid. J. Fluid Mech. 403, 67–88.

Lin, W., Armfield, S.W., 2000b. Direct simulation of weak laminar plane fountains in a homogeneous fluid. Int. J. Heat Mass Transfer 43, 3013–3026.

Nicolette, V.F., Yang, K.T., 1985. Transient cooling by natural convection in a two-dimensional square enclosure. Int. J. Heat Mass Transfer 28, 1721–1732.

Ostrach, S., 1982. Natural convection heat transfer in cavities and cells. In: Proceedings of the Seventh International Heat Transfer Conference, Washington, DC.

Otis, D.R., Roessler, J., 1987. Development of stratification in a cylindrical enclosure. Int. J. Heat Mass Transfer 30, 1633–1636.

Patterson, J.C., Armfield, S.W., 1990. Transient features of natural convection in a cavity. J. Fluid Mech. 219, 469–497.

Patterson, J.C., Imberger, J., 1980. Unsteady natural convection in a rectangular cavity. J. Fluid Mech. 100, 65–86.

Sakurai, T., Matsuda, T., 1972. A temperature adjustment process in a Boussinesq fluid via a bouyancy-induced meridional circulation. J. Fluid Mech. 54, 417–421.

Schladow, S.G., Patterson, J.C., Street, R.L., 1989. Transient flow in a side-heated cavity at high Rayleigh number: A numerical study. J. Fluid Mech. 200, 121–148.

Xin, S., Le Quéré, P., 1995. Direct numerical simulations of two-dimensional chaotic natural convection in a differentially heated cavity of aspect ratio. J. Fluid Mech. 304, 87–118.